# Geophysical Journal International

Advancing Astronomy and Groupsyics

doi: 10.1093/gji/ggz190

Geophys. J. Int. (2019) 219, 94–107 Advance Access publication 2019 May 17 GJI Geodynamics and tectonics

# A new formulation for coupled magma/mantle dynamics

Juliane Dannberg <sup>©</sup>, <sup>1,2</sup> Rene Gassmöller <sup>©</sup>, <sup>1,2</sup> Ryan Grove<sup>3</sup> and Timo Heister <sup>©3,4</sup>

- Department of Earth and Planetary Sciences, University of California, Davis, One Shields Avenue, Davis, CA 95616, USA. E-mail: judannberg@gmail.com
- <sup>2</sup>Department of Geological Sciences, University of Florida, 241 Williamson Hall, PO Box 112120, Gainesville, FL32611-2120, USA.
- <sup>3</sup> School of Mathematical and Statistical Sciences, Clemson University, O-110 Martin Hall, Box 340975, Clemson, SC 29634, USA

Received 2019 April 17; in original form 2018 October 22

#### SUMMARY

Modelling the porous flow of melt through a viscously deforming solid rock matrix is a useful tool for interpreting observations from the Earth's surface, and advances our understanding of the dynamics of the Earth's interior. However, the system of equations describing this process becomes mathematically degenerate in the limit of vanishing melt fraction. Numerical methods that do not consider this degeneracy or avoid it solely by regularizing specific material properties generally become computationally expensive as soon as the melt fraction approaches zero in some part of the domain.

Here, we present a new formulation of the equations for coupled magma/mantle dynamics that addresses this problem, and allows it to accurately compute large-scale 3-D magma/mantle dynamics simulations with extensive regions of zero melt fraction. We achieve this by rescaling one of the solution variables, the compaction pressure, which ensures that for vanishing melt fraction, the equation causing the degeneracy becomes an identity and the other two equations revert to the Stokes system. This allows us to split the domain into two parts: in mesh cells where melt is present, we solve the coupled system of magma/mantle dynamics. In cells without melt, we solve the Stokes system as it is done for mantle convection without melt transport and constrain the remaining degrees of freedom.

We have implemented this formulation in the open source geodynamic modelling code ASPECT and illustrate the improved performance compared to the previous three-field formulation, showing numerically that the new formulation is robust in terms of problem size and only slightly sensitive to model parameters. Beyond that, we demonstrate the applicability to realistic problems by showing large-scale 2-D and 3-D models of mid-ocean ridges with complex rheology. Hence, we believe that our new formulation and its implementation in ASPECT will prove a valuable tool for studying the interaction of melt segregating through and interacting with a solid host rock in the Earth and other planetary bodies using high-resolution, 3-D simulations.

**Key words:** Numerical solutions; Dynamics of lithosphere and mantle; Mechanics, theory, and modelling; Mid-ocean ridge processes; Magma migration and fragmentation.

# 1 INTRODUCTION

Many Earth system processes are controlled by the porous flow of melt through a viscously deforming solid rock matrix. The equations that describe this process have been derived a long time ago (e.g. McKenzie 1984), and they consistently couple viscous mantle deformation (Stokes flow) with Darcy's law for the transport of the fluid (melt; Spiegelman *et al.* 2007). A large number of numerical models have been formulated that use these equations for different application cases (e.g. Katz 2006, 2008; Weatherley & Katz 2012; Keller *et al.* 2013; Butler 2017; Katz *et al.* 2017; Keller *et al.* 2017; Turner *et al.* 2017). However, many formulations of coupled

Stokes/Darcy flow break down in the limit of vanishing melt fraction (or porosity) because for this case the system is mathematically degenerate (Arbogast *et al.* 2017).

A common solution for this problem is introducing a cut-off or regularization for certain material properties or solution variables (Keller *et al.* 2013; Wilson *et al.* 2014; Rhebergen *et al.* 2015; Dannberg & Heister 2016). Regularizing the equations in such a way generally means that either the system does not exactly reduce to the Stokes problem in the case of zero porosity or that the single-phase Stokes problem is solved in parts of the domain that are partially molten. A major drawback of this approach is that numerical methods that do not take into account the degeneracy

<sup>&</sup>lt;sup>4</sup>Scientific Computing and Imaging Institute, University of Utah, 72 S Central Campus Drive, Room 3750, Salt Lake City, UT 84112, USA

of the porosity  $\phi$ , and instead regularize the equations, for example, by imposing a small non-zero porosity everywhere, are sure to have a condition number that grows as the porosity approaches zero (Arbogast *et al.* 2017). This makes it computationally expensive to compute numerical models with regions of vanishing porosity.

Arbogast et al. (2017) address this problem by developing a mixed variational framework, carefully scaling the Darcy variables by powers of the porosity, and defining a mixed finite element method for solving the Darcy–Stokes system. It requires a particular choice of finite elements (of Raviart–Thomas type), and it is based on specific assumptions on how material properties such as the permeability and the bulk viscosity depend on the amount of melt present, as we will discuss in Section 2.

Here, we present a different formulation of the equations for coupled Stokes/Darcy flow that allows for large-scale 3-D magma/mantle dynamics simulations with extensive regions of zero porosity. We have implemented this formulation in the open source geodynamic modelling code ASPECT (Dannberg & Heister 2016; Heister *et al.* 2017; Bangerth *et al.* 2018a,b), which is based on the deal.II finite element library (Bangerth *et al.* 2007; Alzetta *et al.* 2018). Using ASPECT, we have tested the new method on real-world applications, in parallel, and with adaptive mesh refinement.

In the following, we will derive our new formulation and its numerical implementation, and discuss the convergence behaviour that is expected for this method (Section 2). We will demonstrate the correctness of our implementation based on a benchmark case that specifically addresses the boundary between regions with and without melt, and illustrate the improved performance compared to the three-field formulation used in Dannberg & Heister (2016; Section 3.1). Finally, we will show 2-D and 3-D mid-ocean ridge (MOR) models to demonstrate the applicability of our method to earth-like settings (Sections 3.2 and 3.3). The code used to generate these results can be found in the repository at https://github.com/g eodynamics/aspect and all input files to reproduce the results are available at https://github.com/tjhei/paper-aspect-melt-paper-2-dat a.

#### 2 FORMULATION OF THE PROBLEM

We consider the equations describing the behaviour of silicate melt percolating through and interacting with a viscously deforming host rock (e.g. McKenzie 1984):

$$\frac{\partial}{\partial t} \left[ \rho_{\rm f} \phi \right] + \nabla \cdot \left[ \rho_{\rm f} \phi \mathbf{u}_{\rm f} \right] = \Gamma, \tag{1}$$

$$\frac{\partial}{\partial t} \left[ \rho_{s} (1 - \phi) \right] + \nabla \cdot \left[ \rho_{s} (1 - \phi) \mathbf{u}_{s} \right] = -\Gamma, \tag{2}$$

$$\phi\left(\mathbf{u}_{\mathrm{f}} - \mathbf{u}_{\mathrm{s}}\right) = -K_{\mathrm{D}}\left(\nabla p_{\mathrm{f}} - \rho_{\mathrm{f}}\mathbf{g}\right),\tag{3}$$

$$-\nabla \cdot [2\eta \dot{\varepsilon} + \xi(\nabla \cdot \mathbf{u}_{s})\mathbf{1}] + \nabla p_{f} = \bar{\rho}\mathbf{g}. \tag{4}$$

Here,  $\phi$  is the porosity,  $\rho$  is the density,  $\mathbf{u}$  is the velocity,  $\Gamma$  is the melting rate,  $K_{\rm D}$  is the Darcy coefficient, p is the pressure,  $\mathbf{g}$  is the gravity vector,  $\eta$  is the shear viscosity,  $\xi$  is the bulk viscosity and  $\varepsilon = \nabla \mathbf{u}_{\rm s} + (\nabla \mathbf{u}_{\rm s})^{\rm T} - \frac{1}{3}(\nabla \cdot \mathbf{u}_{\rm s})\mathbf{1}$  is the deviatoric strain rate. The index f indicates the melt (fluid), the index s indicates the solid and quantities that are phase-weighted averages between the solid and the fluid are denoted by a bar.

Two important material properties in the context of the transition between solid-state mantle convection and two-phase magma/mantle dynamics are  $K_D$  and  $\xi$ . The Darcy coefficient is defined as the ratio of permeability k and fluid viscosity  $\eta_f$ , and while  $\eta_f$  is often, for simplicity, assumed to be constant, the permeability depends on the porosity in form of a power-law  $k \propto \phi^n$ , where, generally, 2 < n < 3. For low melt fractions, melt forms interconnected tubes along grain edges, leading to a power-law exponent of  $n \approx$ 2, whereas for larger melt fractions, the power-law exponent shifts to  $n \approx 3$  as melt forms thin sheets along grain boundaries (Miller et al. 2014; Rudge 2018a). This means that for vanishing porosity,  $K_{\rm D} \to 0$ . The compaction viscosity  $\xi$  is often assumed to scale as  $\xi \propto \phi^{-1}$ , as suggested, for example, by a homogenization approach (Simpson et al. 2010), so that the matrix cannot be compacted ( $\xi$  $\rightarrow \infty$ ) if no melt is present. More recent studies indicate that the porosity dependence might be weaker, suggesting a relation of  $\xi$  $\propto -\log(\phi)$  for Nabarro-Herring (volume diffusion) creep (Rudge 2018b), and  $\xi \propto \eta$  (except for when  $\phi \ll 0.01$ ) for Coble (grain boundary diffusion) creep (Takei & Holtzman 2009; Rudge 2018b).

Arbogast *et al.* (2017) based their work on the assumptions that  $k = k_0 \phi^{2+2\theta}$  with  $\theta$  a constant between 0 and 1/2, and  $\xi = \eta/\phi$ , which are common relations used in many geodynamic models. In the following, we will discuss the equations above without making specific assumptions about the material properties other than  $k \to 0$  and  $\xi \to \infty$  for  $\phi \to 0$ .

# 2.1 Original formulation used in Dannberg & Heister (2016)

In previous work (Dannberg & Heister 2016), we reformulated the equations by building on the three-field formulation from Keller *et al.* (2013), extending them to compressible solid and fluid phases:

$$-\nabla \cdot (2\eta \dot{\varepsilon}) + \nabla p_{\rm f} + \nabla p_{\rm c} = \bar{\rho} \mathbf{g},\tag{5}$$

$$\nabla \cdot \mathbf{u}_{s} - \nabla \cdot K_{D} \nabla p_{f} - K_{D} \nabla p_{f} \cdot \frac{\nabla \rho_{f}}{\rho_{f}} = -\nabla \cdot (K_{D} \rho_{f} \mathbf{g})$$

$$+ \Gamma \left( \frac{1}{\rho_{f}} - \frac{1}{\rho_{s}} \right)$$

$$- \frac{\phi}{\rho_{c}} \mathbf{u}_{s} \cdot \nabla \rho_{f} - (\mathbf{u}_{s} \cdot \mathbf{g})(1 - \phi) \kappa_{s} \rho_{s} - \mathbf{K}_{D} \mathbf{g} \cdot \nabla \rho_{f},$$

$$(6)$$

$$\nabla \cdot \mathbf{u}_{s} + \frac{p_{c}}{\xi} = 0. \tag{7}$$

All terms that vanish in the limit of zero porosity and no melting are highlighted. This instantaneous problem determining the pressures and velocities of both phases is complemented by an advection equation, covering the evolution of the porosity over time:

$$\frac{\partial \phi}{\partial t} + \mathbf{u}_{s} \cdot \nabla \phi = \frac{\Gamma}{\rho_{s}} + (1 - \phi)(\nabla \cdot \mathbf{u}_{s} + \kappa_{s} \rho_{s} \mathbf{g} \cdot \mathbf{u}_{s}). \tag{8}$$

There are a number of strategies available for solving this advection problem, and in the following, we will focus on the challenges associated with numerically solving eqs (5)–(7). Note, however, that we solve the advection problem (8) separately from the elliptic eqs (5)–(7), and iterate over both systems to solve the nonlinear problem. Consequently, we can assume that we know the distribution of the porosity  $\phi$  when solving eqs (5)–(7).

These equations can be brought into the weak form (see Dannberg & Heister 2016) and solved as outlined in Rhebergen *et al.* (2015). This results in the linear system:

$$\begin{pmatrix} \mathbf{A} & \mathbf{B}^T & \mathbf{B}^T \\ \mathbf{B} & \mathbf{N} & \mathbf{0} \\ \mathbf{B} & \mathbf{0} & \mathbf{K} \end{pmatrix} \begin{pmatrix} \mathbf{U}_s \\ \mathbf{P}_f \\ \mathbf{P}_c \end{pmatrix} = \begin{pmatrix} \mathbf{F} \\ \mathbf{G} \\ \mathbf{0} \end{pmatrix}. \tag{9}$$

**A**, **B**, **N**, **K**, **F** and **G** are defined as in Dannberg & Heister (2016). We mention the original linear system at this point to highlight the differences between this original and our new formulation, and we will come back to it when discussing the linear system in the new formulation (Section 2.2, eq. 16).

This particular three-field formulation of the equations has been used for real-world applications (Keller *et al.* 2013), existing methods for solving it have been developed with large-scale simulations in mind (Rhebergen *et al.* 2015), and it is already integrated and tested with the other features of the convection code ASPECT we use here, such as a deformable free surface, and the advection of chemical species in the solid and melt using fields or particles. For these reasons, we decided to build on this formulation.

But while it allows it to run large-scale, 3-D models of coupled magma/mantle dynamics, the formulation has several shortcomings. The number of linear solver iterations increases with an increasing ratio of compaction viscosity  $\xi$  and shear viscosity  $\eta$ , which corresponds to a decreasing porosity  $\phi$ . In addition, for the limit of  $\phi \to 0$  (which implies  $K_D \to 0$ ), the compaction pressure  $p_c$ is not defined because of the singularity of the compaction viscosity  $\xi$  in this limit. As discussed in Section 2, it is generally assumed that  $\xi \to \infty$  for  $\phi \to 0$ , at least for incompressible models, which make the assumption that  $\kappa_s = 0$ , so that eq. (7) simplifies to  $\nabla \cdot \mathbf{u}_s = 0$  in the limit of zero porosity. In this case, the last two equations of the linear system (9) become linearly dependent (and the whole system is ill-posed), which is also the reason for the increasing number of linear solver iterations that are needed for decreasing porosity values. Indeed, Arbogast et al. (2017) note that all numerical methods that do not specifically take into account the degeneracy of the porosity are sure to have a condition number that grows as the porosity approaches zero.

Consequently, in order to solve the system in spite of this problem, some limit has to be imposed on the compaction viscosity, either in the form of a maximum value, or in the form of a regularization term that is added to the compaction pressure equation. If the cut-off is carefully designed, the contribution it makes could be at or just slightly larger than the solver tolerance, and would not change the physical behaviour of the system in the zero porosity limit (see also Section 2.3). If, on the other hand, the cut-off is the only measure to prevent the increasing solver iteration counts caused by the degeneracy of the system of equations, this implies that it is chosen substantially larger than the solver tolerance. In that case, the stabilization allows it to solve the equations, but the system will not revert to the incompressible one-phase Stokes equations for vanishing porosity, as there will always be a non-zero contribution of the compaction term that is needed to stabilize the system.

#### 2.2 New formulation

To address these problems, we have developed a new formulation that is based on the idea of rescaling solution variables developed in Arbogast *et al.* (2017), but flexible in the choice of parametrization for  $K_D$  and  $\xi$ , and without requiring a specific discretization choice. To address the degeneracy of the system (9), we scale the third equation with a function  $d(\phi)$  that vanishes for  $K_D = 0$ . For simplicity,

we here chose  $d(\phi) = \sqrt{\frac{K_{\rm D}}{K_{\rm D_0}}}$  (for details, see Section 2.3), but we assume that our method also works for other functions that go to zero in the limit of  $\phi \to 0$ . To keep the matrix symmetric, we also replace  $p_{\rm c}$  by  $\bar{p}_{\rm c}$ , using the relation  $p_{\rm c} = d(\phi)\bar{p}_{\rm c}$ .

With this, we arrive at the following, new system of partial differential equations:

$$\begin{split} &-\nabla\cdot(2\eta\dot{\varepsilon})+\nabla p_{\mathrm{f}}+\nabla\left(d(\phi)\bar{p}_{\mathrm{c}}\right)=\bar{\rho}\mathbf{g},\\ &\nabla\cdot\mathbf{u}_{\mathrm{s}}-\nabla\cdot K_{\mathrm{D}}\nabla p_{\mathrm{f}}-K_{\mathrm{D}}\nabla p_{\mathrm{f}}\cdot\frac{\nabla\rho_{\mathrm{f}}}{\rho_{\mathrm{f}}}=-\nabla\cdot(K_{\mathrm{D}}\rho_{\mathrm{f}}\mathbf{g})\\ &+\Gamma\left(\frac{1}{\rho_{\mathrm{f}}}-\frac{1}{\rho_{\mathrm{s}}}\right)\\ &-\frac{\phi}{\rho_{\mathrm{f}}}\mathbf{u}_{\mathrm{s}}\cdot\nabla\rho_{\mathrm{f}}-(\mathbf{u}_{\mathrm{s}}\cdot\mathbf{g})(1-\phi)\kappa_{\mathrm{s}}\rho_{\mathrm{s}}-K_{\mathrm{D}}\mathbf{g}\cdot\nabla\rho_{\mathrm{f}},\\ &d(\phi)\nabla\cdot\mathbf{u}_{\mathrm{s}}+\frac{d(\phi)^{2}\bar{p}_{\mathrm{c}}}{\varepsilon}=0. \end{split}$$

Again, terms that vanish in the limit of zero porosity are marked in the grey boxes. For this new formulation, it becomes apparent that for the limit of  $\phi \to 0$ , the last equation vanishes completely and we recover the Stokes system from the first two equations, as  $\nabla (d(\phi)\bar{p}_c) = 0$  for  $d(\phi) = 0$ :

$$-\nabla \cdot (2\eta \dot{\varepsilon}) + \nabla p_{\rm f} = \bar{\rho} \mathbf{g},$$
  
$$\nabla \cdot \mathbf{u}_{\rm s} = -(\mathbf{u}_{\rm s} \cdot \mathbf{g}) \kappa_{\rm s} \rho_{\rm s}.$$

We can now use the fact that we know the distribution of the porosity when we solve these equations (see Section 2.1). While the (rescaled) compaction pressure  $\bar{p}_c$  is still not defined in the limit of  $\phi \to 0$ , it is also not used anywhere in the system if  $\phi = 0$ . Hence, to make sure that the linear system can be solved, we can constrain the  $\bar{p}_c$  degrees of freedom (DoFs) to  $\bar{p}_c = 0$  in regions where the porosity is below a given threshold. An example for this is given in Fig. 1. Using the relation  $p_c = d(\phi)\bar{p}_c$  allows us to compute the compaction pressure everywhere in the domain, where in the case of zero porosity (which implies  $d(\phi) = 0$ ) the scaling always leads to  $p_c = 0$ . This formulation has the advantage that no additional computational resources are used to solve the coupled Stokes/Darcy system if no melt is present.

By default, we choose this threshold for solving the two-phase flow equations to be equal to the linear solver tolerance (see Sections 2.3 and 3.2.5), which (for default values) corresponds to a porosity three orders of magnitude lower than the reference value. This means that it is a threshold that is only relevant for the discretized equations and does not change the physical behaviour of the model, and we will later show that our formulation allows it to choose much lower values for this threshold (given the porosity is known with sufficient accuracy). On the other hand, a physical threshold for melt transport—the percolation threshold—has been suggested in some studies (e.g. Zhu & Hirth 2003; Cheadle *et al.* 2004). According to these models, melt segregation and compaction only start to occur once the porosity reaches a critical value and pockets of melt become interconnected. Consequently, we allow our threshold to be chosen as a model input parameter.

In the incompressible formulation, which is a good approximation for models that do not span a large depth range and is commonly used for these applications, all terms that contain the solid compressibility or the fluid density gradient vanish:

$$-\nabla \cdot (2\eta \dot{\varepsilon}) + \nabla p_{\rm f} + \nabla (d(\phi)\bar{p}_{\rm c}) = \bar{\rho}\mathbf{g},\tag{10}$$

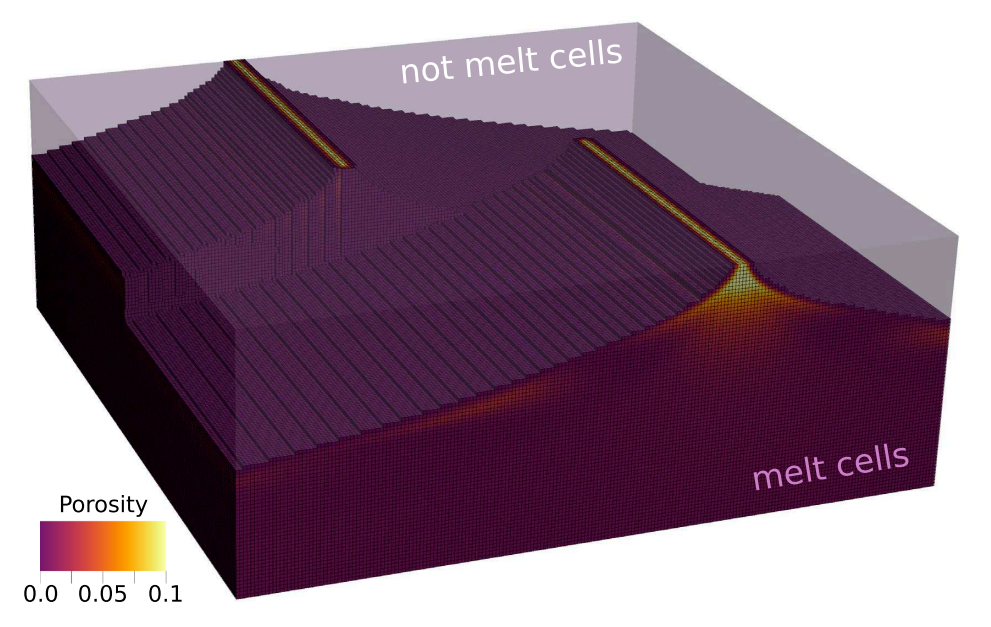


Figure 1. Distribution of melt cells and cells that are not melt cells in a 3-D model of a transform fault. The coupled Stokes—Darcy equations are only solved in cells where the porosity is above a given threshold.

$$\nabla \cdot \mathbf{u}_{s} - \nabla \cdot K_{D} \nabla p_{f} = -\nabla \cdot (K_{D} \rho_{f} \mathbf{g}) + \Gamma \left( \frac{1}{\rho_{f}} - \frac{1}{\rho_{c}} \right), \tag{11}$$

$$d(\phi)\nabla \cdot \mathbf{u}_{s} + \frac{d(\phi)^{2}\bar{p}_{c}}{\xi} = 0.$$
 (12)

The weak form of the full problem is given by finding  $\mathbf{u}_{\mathrm{s}},\,p_{\mathrm{f}},\,\bar{p}_{\mathrm{c}}$  with

$$(2\eta \dot{\varepsilon}(\mathbf{u}_{s}), \dot{\varepsilon}(\mathbf{v}_{s})) - \left(\frac{2}{3}\eta \nabla \cdot \mathbf{u}_{s}, \nabla \cdot \mathbf{v}_{s}\right) - (p_{f}, \nabla \cdot \mathbf{v}_{s}) - (d(\phi)\bar{p}_{c}, \nabla \cdot \mathbf{v}_{s}) = (\bar{\rho}\,\mathbf{g}, \mathbf{v}_{s}),$$
(13)

$$-(\nabla \cdot \mathbf{u}_{s}, q_{f}) - (K_{D} \nabla p_{f}, \nabla q_{f})$$

$$+ \left(K_{D} \nabla p_{f} \cdot \frac{\nabla \rho_{f}}{\rho_{f}}, q_{f}\right) = -(K_{D} \rho_{f} \mathbf{g}, \nabla q_{f})$$

$$+ \int_{\partial \Omega} q_{f} K_{D}(\rho_{f} \mathbf{g} - \mathbf{f}_{2}) \cdot \vec{n} \, ds$$

$$- \left(\frac{1}{\rho_{f}} - \frac{1}{\rho_{s}}\right) (\Gamma, q_{f}) \qquad (14)$$

$$+ \left(\frac{\phi}{\rho_{f}} \mathbf{u}_{s} \cdot \nabla \rho_{f}, q_{f}\right)$$

$$+ ((\mathbf{u}_{s} \cdot \mathbf{g})(1 - \phi) \kappa_{s} \rho_{s}, q_{f})$$

$$+ (K_{D} \mathbf{g} \cdot \nabla \rho_{f}, q_{f}),$$

$$-\left(d(\phi)\nabla \cdot \mathbf{u}_{s}, q_{c}\right) - \left(\frac{1}{\xi}d(\phi)^{2}\bar{p}_{c}, q_{c}\right) = 0. \tag{15}$$

for all test functions  $\mathbf{v}_{s}$ ,  $q_{f}$ ,  $q_{c}$ .

Note that we have made the assumption that at the interface  $\partial \Omega_{\text{melt}}$  between regions where the compaction pressure is constrained to  $p_c$  = 0 and the regions where we solve for the full two-phase system,  $\nabla p_f = \rho_f \mathbf{g}$ . This follows from integration by parts of eq. (12), which

yields

$$\begin{split} -\left(\nabla\cdot\mathbf{u}_{\mathrm{s}},q_{\mathrm{f}}\right)-\left(K_{\mathrm{D}}\nabla p_{\mathrm{f}},\nabla q_{\mathrm{f}}\right) &= -\left(K_{\mathrm{D}}\rho_{\mathrm{f}}\mathbf{g},\nabla q_{\mathrm{f}}\right)-\left(\frac{1}{\rho_{\mathrm{f}}}-\frac{1}{\rho_{\mathrm{s}}}\right)\left(\Gamma,q_{\mathrm{f}}\right) \\ &+\int_{\partial\Omega}q_{\mathrm{f}}K_{\mathrm{D}}(\rho_{\mathrm{f}}\mathbf{g}-\nabla p_{\mathrm{f}})\cdot\vec{n}\;\mathrm{d}s \end{split}$$

for the interface  $\partial \Omega_{\rm melt}$ . As  $K_{\rm D}=0$  in the cells without melt, and  $K_{\rm D}>0$  in the cells where melt is present,  $\int_{\partial \Omega_{\rm melt}} (\rho_{\rm f} {\bf g} - \nabla p_{\rm f}) \cdot \vec{n} \ {\rm d}s = 0$ . Because of Darcy's law (eq. 3), this condition is equivalent to the assumption that the melt velocity equals the solid velocity at the interface between the two regions.

This means in place of eq. (9), we have to solve the linear system:

$$\begin{pmatrix} \mathbf{A} & \mathbf{B}^T & \mathbf{D}^T \\ \mathbf{B} & \mathbf{N} & \mathbf{0} \\ \mathbf{D} & \mathbf{0} & \mathbf{K}' \end{pmatrix} \begin{pmatrix} \mathbf{U}_s \\ \mathbf{P}_f \\ \bar{\mathbf{P}}_c \end{pmatrix} = \begin{pmatrix} \mathbf{F} \\ \mathbf{G} \\ \mathbf{0} \end{pmatrix}, \tag{16}$$

where  ${\bf A}$  is the discretization of  $(2\eta\dot{\varepsilon}({\bf u}_s),\dot{\varepsilon}({\bf v}_s)) - (\frac{2}{3}\eta\nabla\cdot{\bf u}_s,\nabla\cdot{\bf v}_s), {\bf B}$  is given by  $-(p_f,\nabla\cdot{\bf v}_s), {\bf D}$  is a rescaled version of  ${\bf B}$  and given by  $-(d(\phi)p_f,\nabla\cdot{\bf v}_s), {\bf F}$  is given by  $(\bar{\rho}{\bf g},{\bf v}_s), {\bf N}$  is given by  $-(K_D\nabla p_f,\nabla q_f)$  in the incompressible case,  ${\bf G}$  is given by  $-(K_D\nabla p_f,\nabla q_f)$  in the incompressible case,  ${\bf G}$  is given by  $-(K_D\rho_f{\bf g},\nabla q_f) + \int_{\partial\Omega}q_fK_D(\rho_f{\bf g}-{\bf f}_2)\cdot\vec{n}\,{\rm d}s - \left(\frac{1}{\rho_f}-\frac{1}{\rho_s}\right)(\Gamma,q_f)$ 

in the incompressible case and  $\mathbf{K}'$  is given by  $-\left(d(\phi)^2\frac{1}{\xi}\,\bar{p}_{\rm c},\,q_{\rm c}\right)$ . For compressible computations,  $\mathbf{N}$  also contains the non-symmetric, third term from eq. (14), and  $\mathbf{G}$  contains the remaining terms on the right-hand side of eq. (14), which contain  $\kappa_{\rm s}$  and  $\nabla\rho_{\rm f}$ .

As the block structure of the linear system remains the same as in Dannberg & Heister (2016), the same solver strategy, based on Rhebergen *et al.* (2015), can be employed to solve the block system (eq. 16). Specifically, we use flexible GMRES with the block preconditioner (preconditioned from the right):

$$\mathbf{P}^{-1} = \begin{pmatrix} \mathbf{A} & \mathbf{B}^T & \mathbf{D}^T \\ \mathbf{0} & -\frac{1}{\eta} \mathbf{M}_{p_{\mathrm{f}}, p_{\mathrm{f}}} - K_{\mathrm{D}} \mathbf{L}_{p_{\mathrm{f}}} & -\frac{d(\phi)}{\eta} \mathbf{M}_{p_{\mathrm{f}}, p_{\mathrm{c}}} \\ \mathbf{0} & -\frac{d(\phi)}{\eta} \mathbf{M}_{p_{\mathrm{c}}, p_{\mathrm{f}}} & -d(\phi)^2 (\frac{1}{\eta} + \frac{1}{\xi}) \mathbf{M}_{p_{\mathrm{c}}, p_{\mathrm{c}}} \end{pmatrix}^{-1}.$$
(17)

Here,  $[\mathbf{M}_{I,J}]_{i,j} = (\phi_{I,i}, \phi_{J,j})$  are mass matrices between the two finite element spaces (I and J stand for  $p_{\rm f}$  or  $p_{\rm c}$ ;  $\phi_{I,i}$  is the corresponding ith shape function of the space I) and  $[\mathbf{L}_{p_{\rm f}}]_{i,j} = (\nabla \phi_{i,p_{\rm f}}, \nabla \phi_{j,p_{\rm f}})$ 

the stiffness matrix. To simplify the notation, we write the product of the mass and stiffness matrices with a varying coefficient (such as  $\frac{1}{\eta}$ ) as above. In the implementation those coefficients are pulled into the inner products and evaluated by quadrature point.

To solve the linear system, we group the second and third row and column together to get

$$\mathbf{P}^{-1} = \begin{pmatrix} \mathbf{A} & \hat{\mathbf{B}}^T \\ 0 & \mathbf{S} \end{pmatrix}^{-1},$$

where the bottom right  $2 \times 2$  block in (17) is the Schur complement **S**. With this,  $\mathbf{P}^{-1}$  is an upper triangular operator requiring the approximation  $\mathbf{A}^{-1}$  of and  $\mathbf{S}^{-1}$ . We decided to approximate  $\mathbf{A}^{-1}$  using an inner CG solver preconditioned by Trilinos ML applied to the diagonal blocks of **A**. The inner solves with **S** are done using CG preconditioned by Trilinos ML.

# 2.3 Constraining the compaction pressure DoFs

As outlined in Section 2.2, we constrain the compaction pressure DoFs to  $\bar{p}_c = 0$  in regions where the porosity is below a given threshold. We have implemented our formulation using the finite element method, which implies that to be able to find a solution for the compaction pressure, we have to make the same choice for all points in a given mesh cell: either solve the coupled Stokes/Darcy system or constrain the compaction pressure DoFs. Because of that, we base our discussion around mesh cells and use a scaling factor  $d(\phi)$  that is piece-wise constant in each cell. However, our method is not only applicable to finite elements; in the more general case it is important to make sure that in every point where material properties that contribute to the solution of a given  $p_c$  DoF are evaluated, the same choice is made.

In practice, we choose this threshold  $K_{\rm threshold}$  based on the Darcy coefficient  $K_{\rm D}$  relative to a reference value  $K_{\rm D_0}$ , as this ratio is what we use to rescale the different matrix blocks in the linear system (16).  $K_{\rm D_0}$  is defined as the ratio of permeability and fluid viscosity at a porosity that is typical for the model (in the following examples, we will use a value of 1 per cent). But because it is part of ASPECT's 'material model' plugin structure (see Bangerth *et al.* 2018b), different values of  $K_{\rm D_0}$  can be chosen for different application cases. This means that the last equation in (16) will not be rescaled at all if the porosity equals this reference porosity.

As mentioned above, the decision to constrain DoFs is made for each cell, separating the model domain into 'melt cells', where the full equations are solved, and cells that are not 'melt cells' with the compaction pressure DoFs being constrained. An example for this is shown in Fig. 1. A cell is determined to be a 'melt cell' if  $K_D/K_{D_0} > K_{\text{threshold}}$  anywhere in the cell. (In practice, for the discretized equations, we make this decision by evaluating  $K_D/K_{D_0}$ on any point in the cell where we need the material properties to compute the solution to the linear system). The default value is given by  $K_{\text{threshold}} = 10^{-7}$  (the default value of the linear solver tolerance), but it is an input parameter that can be chosen differently in each model (for its influence on solver performance, see Section 3.2.5). Based on this evaluation, a piece-wise constant scaling factor  $d(\phi)$  for the compaction pressure is computed for each cell. In melt cells,  $d(\phi) = \sqrt{\max(K_{D_{\text{mean}}}/K_{D_0}, K_{\text{threshold}})}$ , where  $K_{D_{\text{mean}}}$ is the arithmetic mean of the Darcy coefficient for the respective cell. Taking the maximum of the average scaling factor in the cell and the chosen threshold value  $K_{\text{threshold}}$  provides a minimum value for the scaling factor and guarantees that we avoid the mathematically degenerate region in all quadrature points where we solve

the two-phase flow equations. In cells that are not melt cells, we set  $d(\phi) = 0$ , and all compaction pressure DoFs are constrained to zero. Effectively, this removes the equations for  $\bar{p_c}$  in the Stokes region and for a computation without any melt cells, the linear system and solver cost is effectively equivalent to a standard Stokes solver.

This algorithm is executed once in every time step, after solving the advection equation for the porosity, to make sure that the constraints for system (16) are the same for every nonlinear iteration and that the nonlinear solver converges. To compute the Darcy coefficient in eq. (14), the same threshold is applied:  $K_{\rm D} = \max{(K_{\rm D_{mean}}, K_{\rm threshold} K_{\rm D_0})}$  in melt cells, and zero otherwise.

Dannberg & Heister (2016) used a different threshold to discriminate between model regions with and without melt migration, directly based on the porosity. In their method, the full two-phase flow equations are only solved for  $\phi > \phi_{\rm threshold}$ . Both methods are compared for different threshold values in Section 3.2.5, and—assuming a reference porosity of 0.01 and a permeability  $k \propto \phi^3$ —both thresholds are related as  $\phi_{\rm threshold} = 0.01 K_{\rm threshold}^{1/3}$ .

#### 2.4 Finite element formulation

While our formulation is generally applicable to models of coupled Stokes/Darcy flow, we will discuss the discretization in the context of the finite element method, which is employed by the geodynamic modelling code ASPECT we used for our implementation. Consequently, we still require a choice of finite element spaces for the discrete solution  $(\mathbf{u}_{s,h}, p_{f,h}, p_{c,h}) \in W_h \subset W = H_0^1(\Omega) \times H^1(\Omega) \times L^2(\Omega)$ . This system is analysed in detail in Grove (2017). We use quadrilateral cells and the following, typical polynomial finite element spaces: let  $Q_k$  be the continuous space with tensor-product polynomials of degree k on each cell and let  $DGP_k$  be the discontinuous space with polynomials of degree k.

To be able to solve for a discrete  $p_{c,h}$  in eq. (15), the space needs to be discontinuous to allow a jump from melt to a no-melt cell, so we choose  $DGP_k$ .

In the case  $K_D = 0$  (no melt in the domain), we recover the standard Stokes system and well-posedness requires a stable finite element choice for  $\mathbf{u}_{s,h}$  and  $p_{f,h}$  to guarantee convergence. One example is the usage of Taylor–Hood elements, where the velocity is discretized with one polynomial degree higher than the pressure. Consequently, we choose  $Q_{k+1}$  for each component of the velocity  $\mathbf{u}_{s,h}$ , and use the finite element space  $W_k^L$ :

$$W_k^L = Q_{k+1}^d \times Q_k \times DGP_k.$$

This gives stable solutions and optimal convergence rates for  $K_D = 0$ 

On the other hand, if we consider a situation with melt everywhere  $(K_D \ge K_{D,\min} > 0)$ ,  $W_k^L$  leads to suboptimal convergence rates, and increasing the polynomial order of  $p_{t,h}$  would be beneficial. We note that the inverse of the minimum value of  $K_D$  appears in the stability estimate, confirming the issue of letting  $K_D$  go to zero.

Our simulations in this paper are done with  $W_2^L$ . For the particular three-field form of the partial differential equations, we have adopted here (eqs. 5–7), and the choice of scaling we suggest, alternatives would be to either always require a minimum  $K_D$ , add stabilization terms to make the Stokes solution stable for  $K_D=0$ , or discretize with different finite element spaces in the regions with and without melt.

#### 3 RESULTS

# 3.1 1-D analytical solution for the interface between regions with and without melt

We use a 1-D benchmark from Arbogast *et al.* (2017) to show that our formulation is correct, and that the solver performs much better than the previous one in Dannberg & Heister (2016). The benchmark specifically addresses the transition between regions with both melt and solid, where the coupled Stokes/Darcy system is solved, and regions without melt, where the problem is reduced to the Stokes problem. This is done by choosing the porosity as zero in the upper half of the model domain, and as a quadratic function in the lower half, in such a way that the transition between the two regions is continuous and smooth (Fig. 2). Under the assumption that  $\phi \ll 1$ , Arbogast *et al.* (2017; eqs 6.21–6.23) derive an approximate solution for this given porosity distribution, which we use to compute errors and convergence rates of our method.

Our numerical results show similar convergence rates as Arbogast *et al.* (2017): quadratic convergence for the solid velocity and linear convergence for the fluid and compaction pressure (Fig. 3). Beyond that, we find that the number of linear solver iterations is not sensitive to problem size, and that the iteration count does not vary substantially in dependence of the material properties, such as, for example, the ratio between shear and compaction viscosity (Tables 1 and 2). This is a substantial improvement from the very strong dependence on both problem size and material properties exhibited by the method used in Dannberg & Heister (2016), which is what motivated this study.

# 3.2 Numerical results: 2-D mid-ocean ridge model

In the previous section, we have shown that our formulation correctly reproduces analytical solutions and for simple, 1-D models solver performance is independent of problem size and contrast between shear and compaction viscosity. In the following, we will demonstrate that our implementation also performs well for realistic models of coupled magma/mantle dynamics that are relevant for advancing our understanding of how magma rises from its source region to the surface. For this purpose, we set up a MOR model with a visco-plastic, temperature and porosity-dependent rheology. Prescribed outflow at the side boundaries leads to upward flow beneath the ridge axis, so that inflowing material rises and melts adiabatically below the ridge. We use the melting parametrization from Katz et al. (2003) as depicted in Fig. 4. To track the temperature, the porosity and the degree of melting (depletion), we use second-order finite elements and advect them as fields as described in Dannberg & Heister (2016), Heister et al. (2017) and Bangerth et al. (2018b). The model includes the effect of latent heat of melting and freezing, but does not take into account shear heating or adiabatic heating (Boussinesq Approximation). To stabilize the advection equations, we employ the entropy-viscosity method (Guermond et al. 2011), which evaluates the residual associated with the entropy of the temperature (composition, porosity) equation and adds artificial diffusion based on this residual, so that more diffusion is added in areas where the numerical approximation is poor, such as close to strong gradients (see also Kronbichler et al. 2012, Section 3.2.6).

#### 3.2.1 Boundary conditions

The temperature is fixed to 293 K at the top boundary and to 1570 K at the bottom boundary, while the side boundaries are insulating. Porosity and depletion fields are fixed to zero at the inflow (bottom) boundary, and Neumann boundary conditions are applied at the other boundaries. We prescribe the horizontal component of the velocity to a constant value of 4 cm yr<sup>-1</sup> on the right model boundary to generate passive upwelling of material below the ridge axis and horizontal flow away from the MOR. In addition, the lithostatic pressure is applied as a traction boundary condition for the vertical stress component at the right boundary and the stress at the bottom boundary, allowing free inflow and outflow. The top and left boundaries are free-slip boundaries and are impermeable to the flow of solid material, but melt can leave the domain through the top boundary (see next). Fig. 5 illustrates the set-up.

To allow melt to escape at the ridge axis, we add a temperature perturbation to the otherwise constant boundary temperature at the top of the model in form of a hyperbolic tangent close to the ridge axis. So, the total boundary temperature is defined as

$$T = T_0 + \Delta T \left( 1 - \tanh \left( \frac{x - x_0}{w} \right) \right), \tag{18}$$

with  $T_0 = 293$  K,  $\Delta T = 600$  K,  $x_0 = 2000$  m and w = 1000 m. This leads to a non-zero melt fraction at the ridge axis, where melt can flow out of the model domain. To avoid a suction effect at the ridge axis, we prescribe the fluid pressure gradient at the upper model boundary as

$$\nabla p_{\rm f} = (f \,\rho_{\rm f} + (1 - f) \,\rho_{\rm s}) \,\mathbf{g},\tag{19}$$

similar to the pressure boundary condition applied in Katz (2010) for the same reason. In this expression, f controls the resistance to flow through the boundary: f=0 would allow free outflow of melt like at an open boundary, and f=1 corresponds to a closed boundary. Here, we use f=0.99, which is large enough to let melt flow out of the domain and to limit the steady-state porosity beneath the ridge axis to approximately 10 per cent, but not so large that the outflow dominates the melt flow in the whole melting region.

#### 3.2.2 Material properties

We combine a temperature and porosity-dependent diffusion creep rheology with a stress limiter of the following form:

$$\eta(\phi, T) = \begin{cases} 
\eta_0 e^{-\alpha\phi - \beta(T - T_0)/T_0}, & \text{if } \sigma < \sigma_{\text{yield}} \\ \frac{\sigma_{\text{yield}}}{2\delta tI} & \text{otherwise} 
\end{cases},$$
(20)

where  $\dot{\varepsilon}_{II}$  is the second invariant of the strain rate, and  $\sigma_{\rm yield} = C\cos{(\phi_{\eta})} + p_{\rm s}\sin{(\phi_{\eta})}$  with the cohesion C and the friction angle  $\phi_{\eta}$ . This way, the stress will not exceed the yield strength of the material, and deformation is localized at the ridge axis. The compaction viscosity is given as

$$\xi(\phi, T) = \xi_0 \frac{\phi_0}{\phi} e^{-\beta(T - T_0)/T_0},\tag{21}$$

with the reference porosity  $\phi_0 = 0.05$ .

Most other material properties are chosen as in the MOR model in Katz (2010). The model is incompressible, so that the density is given as

$$\rho = [(\rho_{\rm s} + \Delta \rho_{\rm C} F)(1 - \phi) + \rho_{\rm f} \phi](1 - \alpha_{\rm thermal}(T - T_{\rm ref})), \tag{22}$$

where F is the degree of melting given by the melting parametrization (Katz *et al.* 2003) for the current temperature and pressure

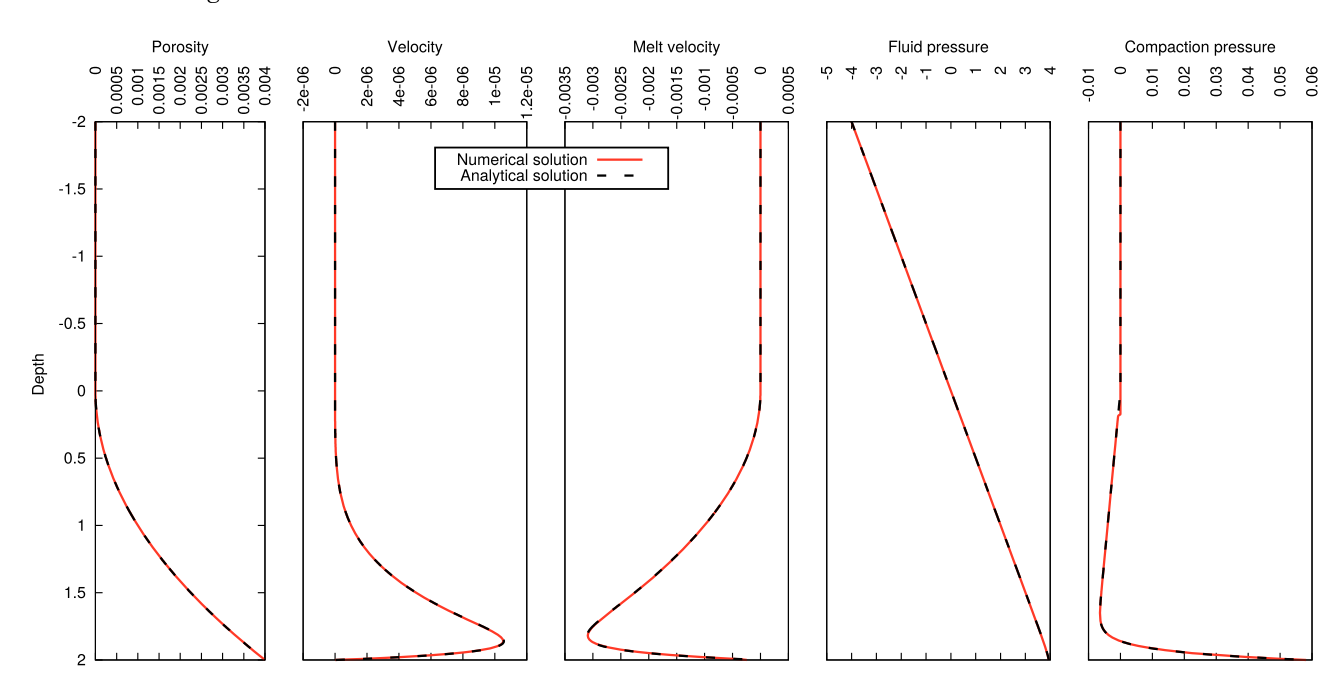


Figure 2. Set-up of the benchmark given in Arbogast et al. (2017). The solution derived in Arbogast et al. (2017) is given as a dashed black line, and the solution computed numerically with ASPECT is marked by a red line.

**Table 1.** Iteration count in dependence of the problem size. While for the method of Dannberg & Heister (2016) the number of iterations increases with the number of degrees of freedom, our new method needs fewer iterations and the iteration count is independent of the problem size.

Problem size: number of linear solver iterations			
#cells	Dannberg & Heister (2016)	This study	
20	107	5	
40	303	7	
80	820	10	
160	No convergence	8	

**Table 2.** Iteration count in dependence of the bulk-to-shear-viscosity ratio, for n = 80 cells in vertical direction.

	Parameters variations: number of linear solv	meters variations: number of linear solver iterations		
$\xi_{\rm max}/\eta$	Dannberg & Heister (2016)	This study		
$10^{1}$	24	11		
$10^{2}$	63	12		
$10^{3}$	214	14		
$10^{4}$	820	16		
$10^{5}$	No convergence	16		
$10^{6}$	No convergence	16		
$10^{7}$	No convergence	11		

(representing depletion of the material),  $\Delta \rho_C$  is the density change due to depletion, and  $\alpha_{thermal}$  is the thermal expansivity. A complete list of input parameters is given in Table 3.

### 3.2.3 Initial conditions

We first run a time-dependent model to generate realistic temperature, composition and porosity distributions for our scaling tests, which are instantaneous.

To prescribe initial conditions for the temperature and composition in the time-dependent model, we use a temperature distribution based on the half-space cooling model to compute the equilibrium melt fraction everywhere in the domain. As we take into account latent heat effects, this initial temperature is reduced in dependence of the amount of melting, and we find the solution iteratively. The resulting temperature is prescribed as initial temperature, and the resulting melt fraction is prescribed as initial depletion. The porosity is assumed to be zero everywhere in the domain at the model start. We first let the model run in a low resolution of 1 km for 3 million years to produce a more realistic temperature and compositional structure that takes into account the dynamic effects of melt transport. Then, we increase the resolution to 550 m throughout the model domain and 270 m within a distance of 7 km around the ridge axis, where melt is extracted from the domain. On this finer mesh, we compute another 3 million years of model evolution, which is approximately the time it takes for solid material to cross the distance from the ridge axis to the far end of the model domain. Finally, we let the model evolve for another 8000 yr ( $\sim$ 370 time steps) with a uniform cell size of 140 m. This allows us to export the final state of the model to data files and use them to create high-resolution initial conditions for the model runs presented in the following. The data files are freely available at https://github.com/tjhei/paper-aspect-melt-paper-2-data together with the input files and allow it to reproduce our results.

#### 3.2.4 Influence of problem size

To show that iteration numbers of the linear solver do not vary substantially with the size of the problem we are solving, we used the data files created from the final state of the 2-D MOR model described above to compute instantaneous flow models with different resolutions (Fig. 7). Our results (see Table 4) show that the number of GMRES iterations is insensitive to the problem size, and the number of Schur complement iterations that are done per GMRES iteration only increases slightly with problem size. This result highlights the usefulness of our new method for large-scale magma/mantle dynamics models.

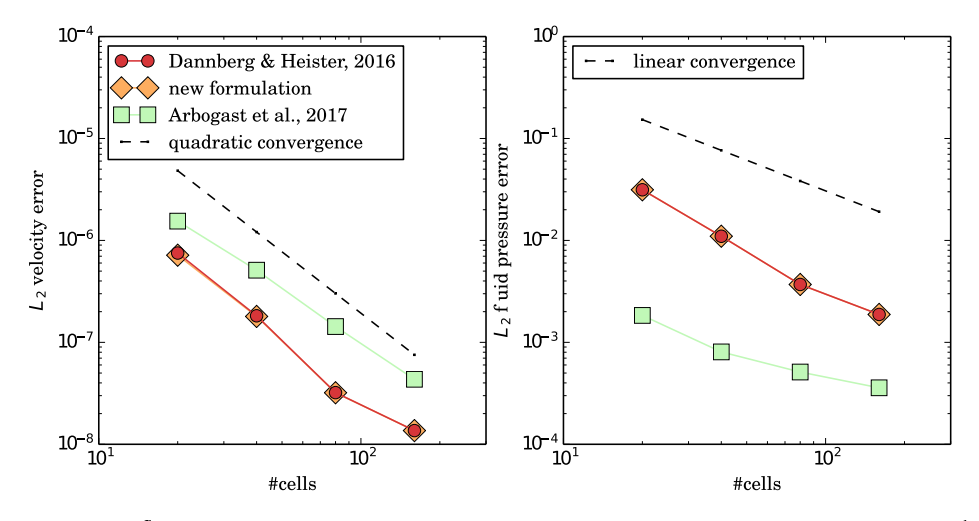
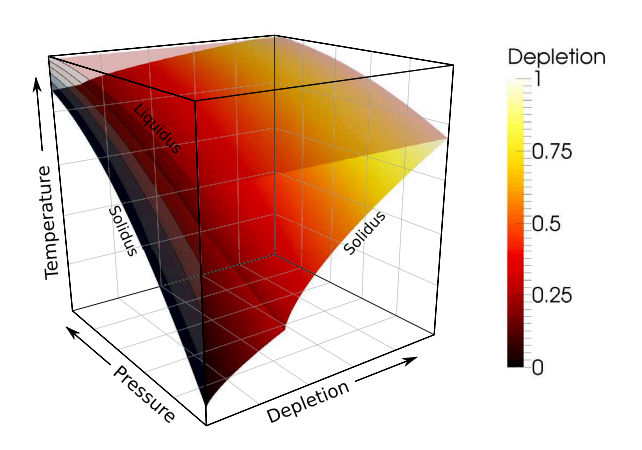


Figure 3. Error for solid velocity and fluid pressure. Results from Arbogast *et al.* (2017). Tables 5 and 6 are plotted for comparison. For the method of Dannberg & Heister (2016), the linear solver does not converge for a resolution higher than n = 80, so the results shown are using a direct solver.



**Figure 4.** Melting parametrization from Katz *et al.* (2003). Shown is a temperature range from 1300 to 2300 K and a pressure range from 0 to 10 GPa. The kink signifies the exhaustion of clinopyroxene in the host rock. Contours between solidus and liquidus in the temperature–pressure plane are drawn at melt fractions of 0, 20, 40, 60, 80 and 100 per cent.

# 3.2.5 Influence of material properties

Rhebergen et al. (2014) and Rhebergen et al. (2015) have identified the ratio of compaction to shear viscosity as a key control on the rate of convergence of the iterative solver for the linear system we solve. Because the compaction viscosity is inversely proportional to the porosity, this ratio increases with decreasing porosity and becomes infinity in the limit of  $\phi \to 0$  (which is the mathematically degenerate case) at the boundaries between regions with and without melt

As this boundary is present in most models of magma/mantle dynamics, and has the potential to slow down convergence of the linear solver substantially, we investigate the dependence of the convergence rate on the compaction-to-shear-viscosity ratio. In our new formulation, we address the part of the problem that relates to the interface between the solid and the partially molten region by rescaling the equation that contains the compaction viscosity, and introducing a threshold for the onset of two-phase flow. Hence, in the following we will test the sensitivity of the iteration count to both the global compaction-to-shear-viscosity ratio and the choice of the melt transport threshold.

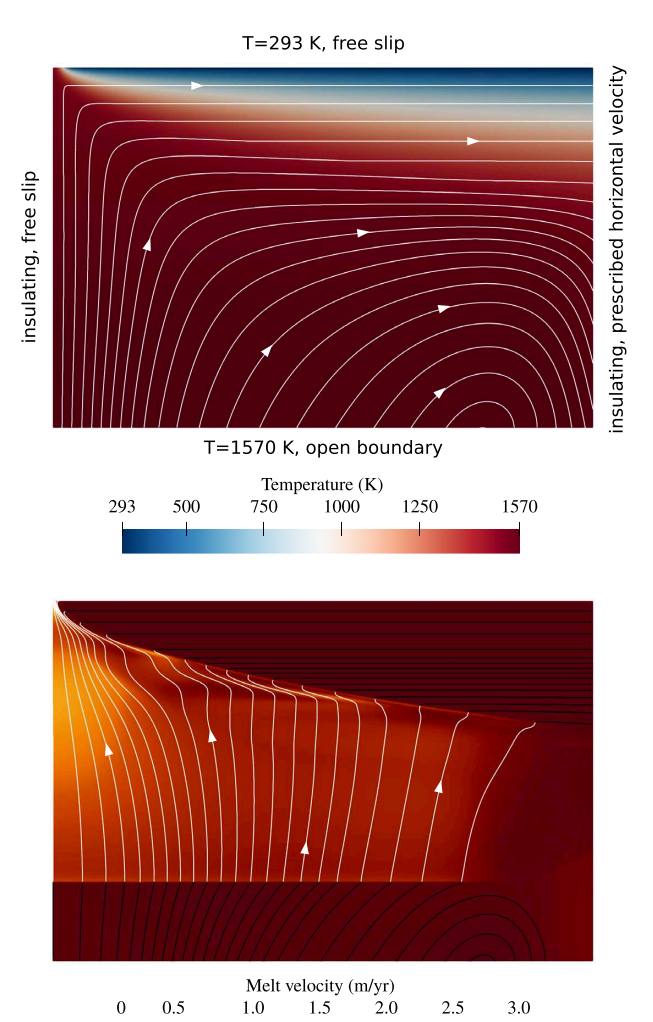


**Figure 5.** Set-up of the mid-ocean ridge model. The top panel illustrates the boundary conditions, temperature distribution and solid velocity (the white streamlines), the bottom panel shows the melt velocity in melt cells (the white streamlines) and in cells that are not melt cells (the black streamlines).

**Table 3.** Parameters used for the mid-ocean ridge models.

Quantity	Value	Reference
Reference bulk viscosity ξ <sub>0</sub>	$4 \times 10^{20}  \mathrm{Pas}$	Katz (2010), maximum value
Reference shear viscosity $\eta_0$	$10^{18} \text{ Pas}$	Katz (2010), preferred value
Melt viscosity $\eta_f$	1 Pas	Katz (2010)
Solid density $\rho_s$	$3000 \; \mathrm{kg} \; \mathrm{m}^{-3}$	Katz (2010)
Fluid density $\rho_{\rm f}$	$2500 \text{ kg m}^{-3}$	Katz (2010)
Compositional density contrast $\Delta \rho_{\rm C}$	$500 \text{ kg m}^{-3}$	a
Reference per meability $k_0$	$10^{-7} \text{m}^2$	Katz (2010), preferred value
Reference porosity $\phi_0$	0.05	Katz (2010)
Melt weakening parameter α	27	Katz (2010)
Temperature weakening parameter $\beta$	24	Hirth & Kohlstedt (2004) <sup>b</sup>
Thermal expansivity α <sub>thermal</sub>	$2 \times 10^{-5} \mathrm{K}^{-1}$	Dannberg & Heister (2016)
Specific heat $C_p$	$1250 \mathrm{Jkg^{-1}\ K^{-1}}$	Dannberg & Heister (2016)
Reference temperature $T_{\text{ref}}$	1600 K	Dannberg & Heister (2016)
Thermal conductivity $k_{\text{thermal}}$	$4.7~{\rm W}~{\rm m}^{-1}~{\rm K}^{-1}$	Dannberg & Heister (2016)
Cohesion C	$2 \times 10^7 \text{ Pa}$	Glerum et al. (2018), table B2
Friction angle $\phi_{\eta}$	$30^{\circ}$	Glerum et al. (2018), table B2
X extent	105 km	_
Z extent	70 km	_

 $<sup>^{</sup>a}\Delta\rho_{\rm C}=500~{\rm kg~m^{-3}}$  leads to a chemical density contrast of approximately 2 per cent for material in the lithosphere, which has a depletion F of 10–15 per cent in our models.

**Table 4.** Iteration counts for a linear solver tolerance of  $10^{-14}$ .

Problem size: number of linear solver iterations			
#cells	GMRES iterations	Average S block iteration	
6144	213	157	
24 576	176	199	
98304	118	229	
393 21 6	118	261	
1572 864	116	308	
6291 456	119	343	

**Table 5.** Iteration counts for a linear solver tolerance of  $10^{-14}$ , and 887 939 Stokes degrees of freedom (98 304 mesh cells).

Compaction-to-shear-viscosity ratio: number of linear solver iterations				
$\xi/\eta  (\phi = 1.5\%)$	GMRES iterations	Average S block iterations		
$2 \times 10^{1}$	74	116		
$2 \times 10^{2}$	1 24	147		
$2 \times 10^{3}$	1 24	248		
$2 \times 10^{4}$	125	345		
$2 \times 10^{5}$	175	403		
$2 \times 10^{6}$	182	434		
$2 \times 10^{7}$	183	435		

For this purpose, we use the same set-up as described above in Section 3.2.4 to compute instantaneous flow models. When the compaction-to-shear-viscosity ratio  $\xi/\eta$  is varied globally (Table 5), we see that there is a weak dependence of the GMRES iteration count on the compaction-to-shear-viscosity ratio, similar to the results of Rhebergen *et al.* (2015). In addition, the S block iteration count increases with  $\xi/\eta$ . This is expected, as our formulation only addresses the increase of  $\xi$  as the porosity  $\phi \to 0$ . However, this sensitivity to  $\xi/\eta$  might not be problematic for realistic applications, as this ratio is expected to be on the order of 1–100 (Hewitt & Fowler 2008; Takei & Holtzman 2009; Katz 2010; Simpson *et al.* 2010; Schmeling *et al.* 2012; Alisic *et al.* 2014).

Note that the values  $\xi/\eta$  given in Table 5 correspond to the ratio of the shear and compaction viscosity for a porosity  $\phi = 0.015$ . The actual ratio in the model varies by two orders of magnitude upwards from this reference value due to the different dependencies on porosity, which means that the ratio increases both for very low and very high porosities.

In addition, we also test the sensitivity of the solver convergence rate to the increase in the compaction-to-shear-viscosity ratio as  $\phi \to 0$  by varying the threshold for the onset of two-phase flow. The results (Table 6) reveal no sensitivity of the GMRES iteration count and only a very weak sensitivity of the S block iteration count to this threshold.

Finally, we also want to provide a direct comparison to the method of Dannberg & Heister (2016). Due to the strong dependence on problem size, we had to reduce the resolution, increase the threshold for the onset of two-phase flow and increase the solver tolerance of the model for this comparison, and we also removed the temperature dependence of viscosity. The results in Table 7 show both overall lower iteration counts and lower sensitivity to model parameters for the formulation developed in this study. They highlight that also for realistic application cases such as melt migration below MORs; our new method performs substantially better than the one developed in Dannberg & Heister (2016), and is feasible for accurately modelling the interface between regions with and without melt.

# 3.2.6 Scaling behaviour of the implemented solver

In practice, not only the number of iterations, but also the wall clock time per iteration controls the computational cost of a model time step. Therefore, we present scaling tests for the models of this section and Section 3.3 in Fig. 6. All scaling tests were done on Intel Xeon (Skylake) cores connected by an Intel Omnipath network at the Stampede 2 system of the Texas Advanced Computing Center (TACC).

 $<sup>^{</sup>b}\beta = 24$  leads to the same magnitude of temperature dependence as using an Arrhenius model with the activation energy of  $3.75 \times 10^{5}$  J mol<sup>-1</sup> given in Hirth & Kohlstedt (2004) for diffusion creep in olivine.

**Table 6.** Iteration counts for a linear solver tolerance of  $10^{-7}$  (left-hand columns), and  $10^{-14}$  (right-hand columns), using 887939 Stokes degrees of freedom (98 304 mesh cells) and a varying  $K_{\text{threshold}}$ . Note how  $K_{\text{threshold}}$  can be chosen arbitrarily small as it is just a semantic interpretation (where is melt) instead of a numerical necessity to ensure solver convergence.

Threshold for melt transport: number of linear solver iterations				
$K_{ m threshold}$	GMRES solver tolerance 10 <sup>-7</sup>		GMRES solver tolerance 10 <sup>-14</sup>	
	GMRES iterations	Avg. S block iterations	GMRES iterations	Avg. S block iterations
$\overline{10^{-6}}$	37	230	114	252
$10^{-8}$	37	230	114	253
$10^{-10}$	37	239	113	261
$10^{-12}$	37	242	113	269
$10^{-14}$	37	275	115	361

**Table 7.** Iteration counts for a linear solver tolerance of  $10^{-8}$ , and 62404 Stokes degrees of freedom (6144 mesh cells). Entries marked with '-' indicate that there was no convergence reached after  $100\,000\,\text{GMRES}$  iterations.

$K_{ m threshold}$		Dannberg & Heister (2016)		This study	
	$\phi_{ m threshold}$	GMRES iterations	Avg. S block iterations	GMRES iterations	Avg. S block iterations
$\frac{10^{0}}{10^{0}}$	$10^{-2}$	1496	10	69	27
$10^{-2}$	$2.15 \times 10^{-3}$	3471	10	69	156
$10^{-4}$	$4.64 \times 10^{-4}$	12600	10	69	181
$10^{-6}$	$10^{-4}$	42 272	10	69	184
$10^{-8}$	$2.15 \times 10^{-5}$	95 869	10	69	190
$10^{-10}$	$4.64 \times 10^{-6}$	_	=	70	192

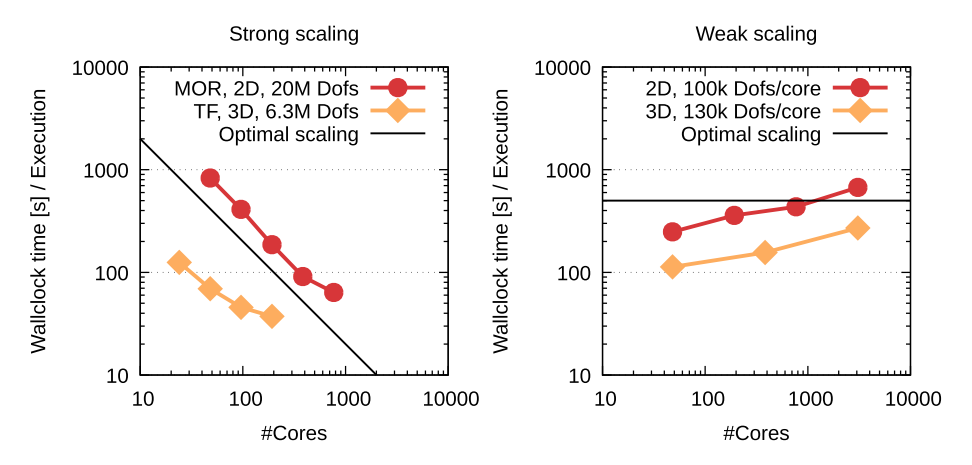


Figure 6. Strong and weak scaling results for the 2-D mid-ocean ridge (MOR) model described in Section 3.2 and the 3-D transform fault (TF) model described in Section 3.3. The presented values represent the time required for solving the combined Stokes/Darcy equations once (i.e. without time spent for assembly, and equations for temperature, composition and porosity). Note that the two model series use different iterative solver tolerances and values for  $K_{\text{threshold}}$ , so that absolute wall clock times cannot be compared between 2-D and 3-D. The scaling behaviour is not affected by these choices.

Both models show a linear strong scaling to about 50 000 DoFs per core (considering only solid velocity, fluid pressure and compaction pressure DoFs); beyond that the efficiency drops significantly. The weak scaling results suggest a slightly less than optimal, but still acceptable scaling with model size, which leads to an increase of Stokes solver time by about a factor of 2.7 when increasing the model size by a factor of 64 (from 5 million DoFs to 327 million DoFs in 2-D, and from 6 million DoFs to 396 million DoFs in 3-D). These results are consistent with the slight increase in Schur complement iterations with model size discussed in Section 3.2.4 and show that our solver scales reasonably well to problem sizes of several hundred million and potentially a few billion DoFs, although there is still room for optimization.

### 3.2.7 A note on mesh refinement

In Dannberg & Heister (2016), we discussed some strategies for adaptively refining the mesh in models with coupled magma/mantle dynamics. They mainly focused on refining the mesh based on solution variables or material properties. However, one can think of other useful mesh refinement strategies: one alternative is to just refine all cells where melt is present. Another natural criterion that comes to mind is the intrinsic length scale of melt migration: the compaction length. The compaction length is defined as  $\delta_{\rm c} = \sqrt{(\xi + 4\eta/3)K_{\rm D}}$  and is the length scale over which the compaction pressure responds to variations in fluid flux (Spiegelman et al. 2007; McKenzie 1984; Spiegelman 1993). Hence, this length scale should be well resolved in numerical models that consider

the compaction of partially molten rock. As the compaction length varies spatially and temporally, depending on the porosity of the rock and the material properties, adaptive mesh refinement can be a useful tool to make sure that the compaction length is resolved in an evolving model, while simultaneously saving computational resources by coarsening the mesh in regions with a larger compaction length.

We implemented both mesh refinement strategies: one that refines all 'melt cells', and one that adapts the size of the grid cells depending on the local compaction length, allowing it to define the minimum number of cells per compaction length that should be present in the model. However, it becomes apparent that both of these strategies are inferior to refining based on solution variables, at least if the model output of interest is directly related to the solution variables (Fig. 8). Refining in 'melt cells' performs slightly better than global refinement, but not nearly as well as refining based on the porosity or the melt velocity, and using the compaction length as a refinement criterion is inferior even to refining globally. The reason for that is that the compaction length decreases with decreasing melt fraction, due to the strong porosity dependence of the permeability  $(k \propto \phi^n$ , where, generally, 2 < n < 3) and hence  $K_D$ . Accordingly, the highest level of mesh refinement is applied at the boundaries of the melting region where porosities are low and the melt velocity is almost identical to the solid velocity. This increases the number of DoFs, but does not accurately resolve the melt flux in regions where the porosity is large.

The compaction length can be a useful criterion to estimate an upper limit for the length scales of features emerging in a two-phase flow model, and can be used to set a minimum resolution in the partially molten regions. But just resolving the compaction length is generally not sufficient for accurately modelling of two-phase flow. Other physical processes (e.g. related to energy transport or the melting process) may also control the emerging length scales, and previous resolution tests have suggested that accurately modelling processes such as the formation of melt bands requires on the order of 15 grid cells per wavelength of the feature (Katz & Takei 2013). This agrees with our results, where the compaction length (assuming a reference porosity of 0.5 per cent) is on the order of 10 km, which is well resolved in all models in Fig. 8, as the coarsest resolution is 2 km. But because of features on substantially smaller scales than the compaction length our models require a global resolution of 140 m to reach an error of 1 per cent for the global melt flux, which corresponds to  $\sim$ 70 mesh cells per compaction length, or  $\sim$ 15 mesh cells across the sublithospheric decompaction channel.

### 3.3 3-D Application: oceanic transform fault

To show the capability of our method to solve large-scale 3-D problems of coupled magma/mantle dynamics, we present an instantaneous MOR model that includes two ridge segments offset by a transform fault. We generated the initial conditions for this set-up from the end state of the 2-D MOR model by mirroring the distribution of temperature, depletion and porosity with respect to the ridge axis and extending it uniformly in the third dimension, except for an offset of the ridge axis of 40 km in the centre of the model. The material properties and boundary conditions are identical to the 2-D model described in Section 3.2, and the new model boundaries at the front and back are free slip boundaries. The model extents are  $170 \times 170 \times 70$  km, and we solve the (time-independent) coupled Stokes/Darcy equations on approximately 8.9 million cells (262 million DoFs combined for solid velocity, fluid pressure and

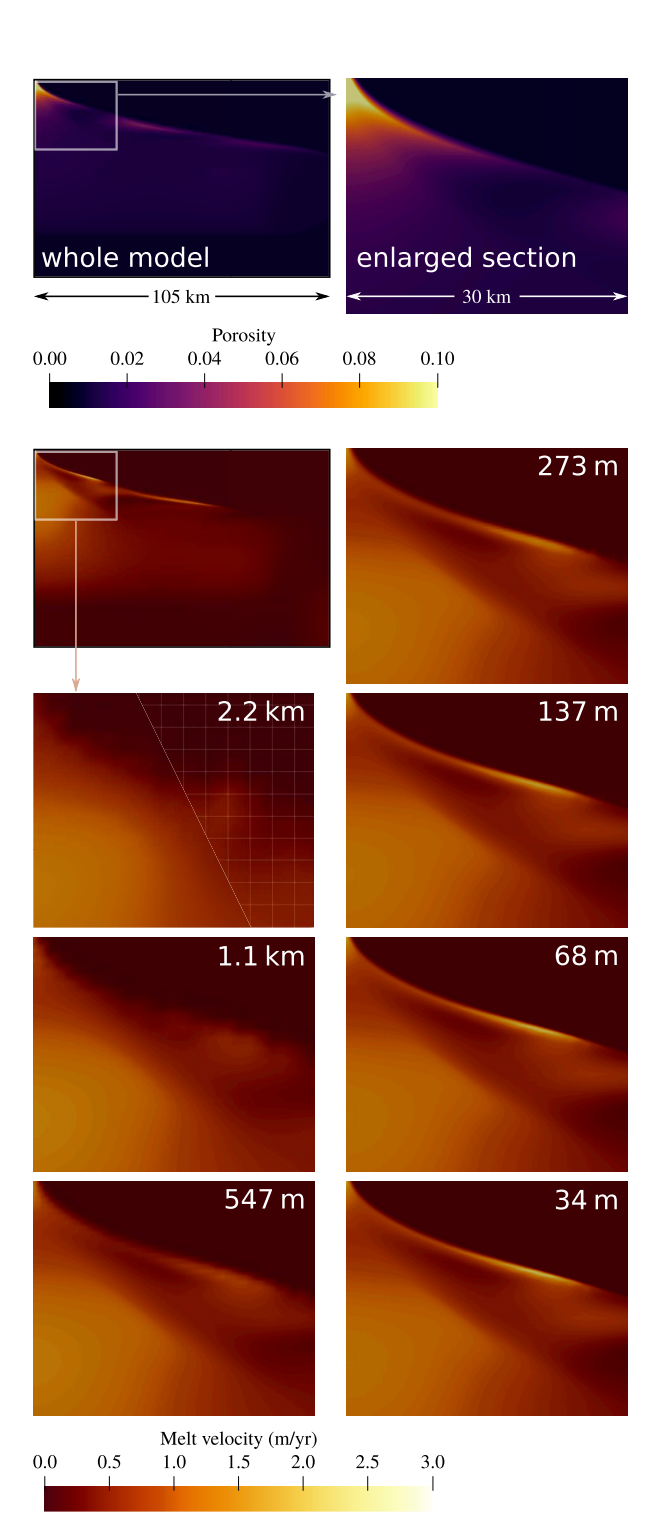


**Figure 7.** Porosity (top row) and melt velocity (all rows below) in a 2-D mid-ocean ridge model for different resolutions as given in Table 4. The panels with a black frame show the whole model, all other panels show the part of the model closest to the ridge axis. Resolution increases as specified by the white labels indicating the cell size in each model.

compaction pressure), as visualized in Fig. 1. We use adaptive mesh refinement to increase the resolution in areas where melt is present, resulting in a cell size of approximately 550 m.

Modelling the flow of melt beneath transform faults has been used as a tool to explain observed changes in crustal thickness where MOR segments are offset by transform faults. Due to the

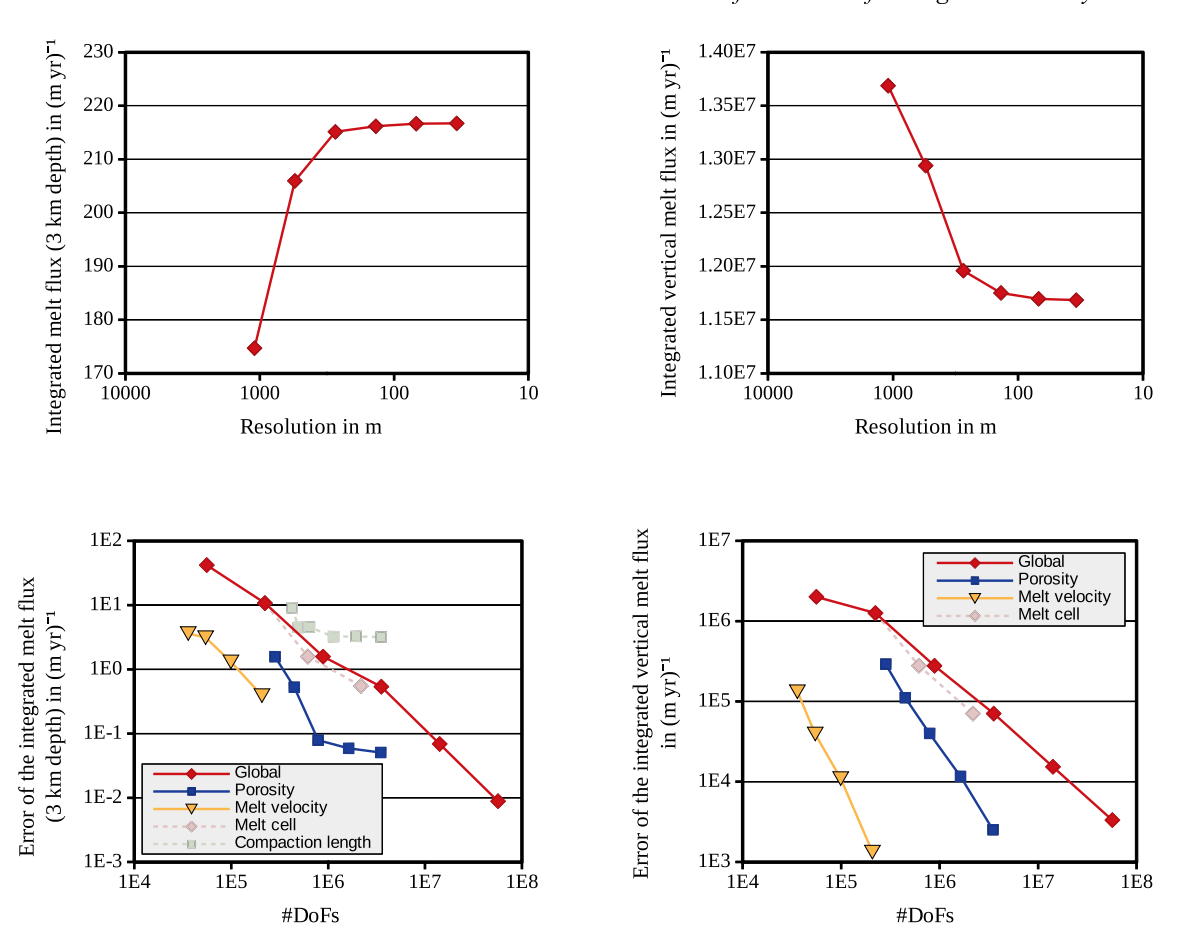


Figure 8. Melt flux in a 2-D mid-ocean ridge model for different resolutions. The top row shows the vertical melt flux integrated over a horizontal line in 3 km depth (left) and the vertical melt flux integrated over the whole model domain (right) for models with uniform refinement of the mesh. The bottom row panels feature the same quantities as the corresponding panels above, only that they show the error from the Richardson extrapolation of the data in the top row in logarithmic scale. The different data series represent uniform mesh refinement (the red diamonds), and adaptive mesh refinement based on the porosity (the blue squares) and the melt velocity (the yellow triangles), both using the Kelly error estimator, the presence of melt (the light red diamonds) and the compaction length (the light green squares). The results show that using adaptive mesh refinement can yield the same accuracy while using 1 to 2 orders of magnitude fewer degrees of freedom, and that for globally integrated quantities, such as the integrated melt flux, it can also yield a higher order of convergence.

high computational costs of 3-D simulations of coupled Stokes—Darcy flow, these models have often used a simplified model of melt transport as suggested by Sparks & Parmentier (1991): melt segregates upwards vertically until it reaches the base of the lithosphere, which acts as in an impermeable boundary. It then migrates along the steepest slope of this boundary until it approaches the ridge axis, where it is extracted to the surface (e.g. Gregg *et al.* 2009; Weatherley & Katz 2010; Hebert & Montési 2011; Bai & Montési 2015).

These models have been used to explain a range of observations, such as differences in axial depth and crustal thickness of ridge segments separated by transform faults (Weatherley & Katz 2010), or crustal thickness variations within intratransform spreading centres (Gregg et al. 2009; Hebert & Montési 2011), and the focusing trajectories predicted by these studies (using Sparks & Parmentier 1991's approach) seem to provide a reasonable approximation to the melt flow predicted by a model of coupled Stokes—Darcy flow (Fig. 9, top right). On the other hand, our model results (Fig. 9, left) show that melt migration may not always follow the slope of the base of the lithosphere. Even though the temperature and porosity fields are symmetric with respect to the respective ridge axis of the individual ridge segments, the flow field evinces 3-D structures. Melt may be focused towards the ridge axis of the opposite ridge

segment over distances of tens of kilometres if that one is closer than the axis of the ridge segment the melt was generated at. Hence, melt crosses the transform fault, and the melt flux along the ridge axis decreases with increasing distance from the fault. In addition, deformation is not only localized at the two ridge segments, but the employed stress-limiter rheology also leads to localization at the transform fault, where no melt is reaching the surface. It is clear that individual features of the flow field are likely to be different in a model with time evolution, where melt pathways are influenced by the acting stresses. However, our results highlight that high-resolution time-dependent 3-D models have a large potential to advance our understanding of the influence of transform faults and oblique spreading directions on the focusing of melt towards the ridge axis, and it is feasible to compute such models with the formulation we developed here.

# 4 CONCLUSIONS

We have developed a new formulation of the governing equations of magma/mantle dynamics that allows it to efficiently model the problem, even in the case of vanishing porosity and large ratios of compaction and shear viscosity. We achieve this by rescaling one of the solution variables, the compaction pressure, with the square root

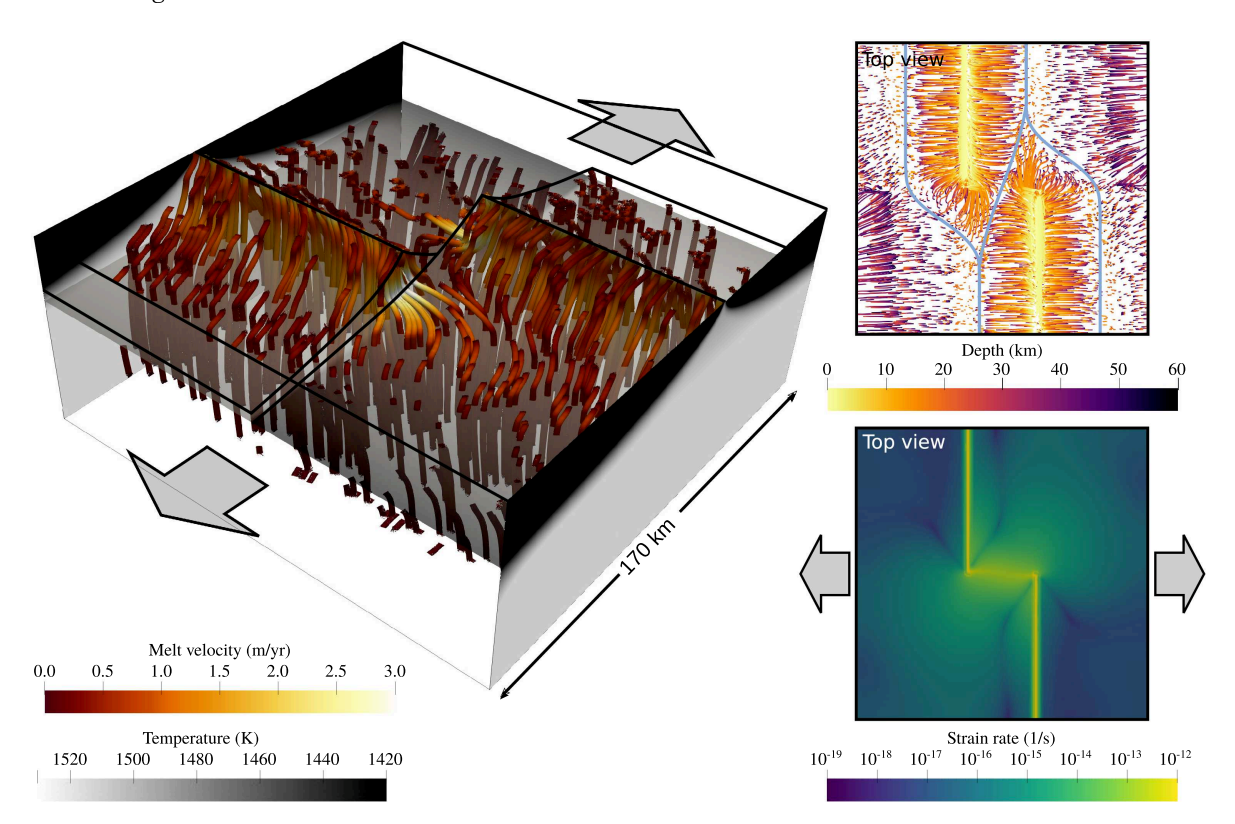


**Figure 9.** Visualization of a 3-D model of two mid-ocean ridge segments separated by a transform fault. The red-to-yellow streamlines show the melt velocity, highlighting the 3-D structure of the flow field (the curved yellow—white streamlines cross the transform fault). The black-to-white background colours indicate temperature and the grey arrows illustrate the prescribed spreading direction. The two insets show the pathways of melt, with the blue lines indicating the regions melt would be focused from to the ridge segments (top), and the deformation at the surface of the model (bottom).

of the Darcy coefficient, and constraining the compaction pressure DoFs to zero for very small porosities. This makes the linear system well posed, even for small or vanishing porosities.

Our numerical results show that the number of linear solver iterations is independent of the problem size, and that there is only a mild sensitivity to the model parameters. Hence, the method can be applied throughout a wide parameter range. Scaling tests reveal that our solver scales reasonably well to problem sizes of several hundred million, and potentially up to a few billion DoFs. Most importantly, the solver convergence does not change with decreasing porosity, when the interface between solid and partially molten regions is approached.

Finally, we demonstrated that our new formulation is suitable for modelling large-scale realistic problems of magma/mantle dynamics, such as melt generation and transport beneath MORs. Hence, we are confident that our new formulation and its implementation in the open source geodynamic modelling software ASPECT will prove most valuable for exploring the interactions of solid rock deformation and melt generation and transport in three dimensions.

# ACKNOWLEDGEMENTS

The authors thank Richard Katz, Dave May and an anonymous reviewer for their helpful comments, which greatly helped to improve this manuscript.

The authors thank the Isaac Newton Institute for Mathematical Sciences for its hospitality during the programme Melt in the Mantle, which was supported by EPSRC grant EP/K032208/1.

All authors were partially supported by the Computational Infrastructure for Geodynamics initiative (CIG), through the National Science Foundation under Awards Nos. EAR-0949446 and EAR-1550901, administered by the University of California-Davis. TH was partially supported by the National Science Foundation awards DMS-1522191, DMS-1901529 and OAC-1835452 and by Technical Data Analysis, Inc. through US Navy SBIR N16A-T003. JD and RG were partially supported by the National Science Foundation under award OCI-1148116 as part of the Software Infrastructure for Sustained Innovation (SI2) program. JD gratefully acknowledges the support of the Deep Carbon Observatory. The authors acknowledge the TACC (http://www.tacc.utexas.edu) at the University of Texas at Austin for providing high-performance computing resources that have contributed to the research results reported within this paper. Clemson University is acknowledged for generous allotment of compute time on the Palmetto cluster.

The authors greatly appreciate all of these sources of support.

# REFERENCES

Alisic, L., Rudge, J.F., Katz, R.F., Wells, G.N. & Rhebergen, S., 2014. Compaction around a rigid, circular inclusion in partially molten rock, J. geophys. Res., 119(7), 5903-5920.

Alzetta, G. et al., 2018. The deal.II library, version 9.0, J. Numer. Math., **26**(4), 173–183.

Arbogast, T., Hesse, M.A. & Taicher, A.L., 2017. Mixed methods for twophase Darcy–Stokes mixtures of partially melted materials with regions of zero porosity, *SIAM J. Sci. Comput.*, **39**(2), B375–B402.

Bai, H. & Montési, L.G., 2015. Slip-rate-dependent melt extraction at oceanic transform faults, *Geochem. Geophys. Geosyst.*, 16(2), 401–419. Bangerth, W., Hartmann, R. & Kanschat, G., 2007. Deal.II—a general-

purpose object-oriented finite element library, *ACM Trans. Math. Softw.*, **33**(4), 24/1–24/27.

- Bangerth, W., Dannberg, J., Gassmoeller, R. & Heister, T., 2018a. ASPECT v2.0.0 [software].
- Bangerth, W., Dannberg, J., Gassmöller, R. & Heister, T., 2018b, ASPECT: Advanced Solver for Problems in Earth's ConvecTion, User Manual, Davis, CA.
- Butler, S., 2017. Shear-induced porosity bands in a compacting porous medium with damage rheology, *Phys. Earth planet. Inter.*, **264**, 7–17.
- Cheadle, M., Elliott, M. & McKenzie, D., 2004. Percolation threshold and permeability of crystallizing igneous rocks: the importance of textural equilibrium, *Geology*, 32(9), 757–760.
- Dannberg, J. & Heister, T., 2016. Compressible magma/mantle dynamics: 3-D, adaptive simulations in aspect, *Geophys. J. Int.*, **207**(3), 1343–1366.
- Glerum, A., Thieulot, C., Fraters, M., Blom, C. & Spakman, W., 2018. Nonlinear viscoplasticity in aspect: benchmarking and applications to subduction. *Solid Earth*, 9(2), 267–294.
- Gregg, P.M., Behn, M.D., Lin, J. & Grove, T.L., 2009. Melt generation, crystallization, and extraction beneath segmented oceanic transform faults, J. geophys. Res., 114(B11).
- Grove, R.R., 2017. Discretizations & efficient linear solvers for problems related to fluid flow, *PhD thesis*, Clemson University.
- Guermond, J.-L., Pasquetti, R. & Popov, B., 2011. Entropy viscosity method for nonlinear conservation laws, J. Comput. Phys., 230, 4248–4267.
- Hebert, L.B. & Montési, L.G., 2011. Melt extraction pathways at segmented oceanic ridges: application to the east pacific rise at the siqueiros transform, *Geophys. Res. Lett.*, 38(11).
- Heister, T., Dannberg, J., Gassmöller, R. & Bangerth, W., 2017. High accuracy mantle convection simulation through modern numerical methods—ii: realistic models and problems, *Geophys. J. Int.*, **210**(2), 833–851.
- Hewitt, I. & Fowler, A., 2008. Partial melting in an upwelling mantle column, Proc. R. Soc. A. 464, 2467–2491.
- Hirth, G. & Kohlstedt, D., 2004. Rheology of the upper mantle and the mantle wedge: a view from the experimentalists, , Eiler, J.in *Inside the* Subduction Factory, Vol. 138, pp. 83–105, AGU.
- Katz, R.F., 2006. The dynamics of melt and shear localization in partially molten aggregates, *Nature*, 442, 676–679.
- Katz, R.F., 2008. Magma dynamics with the enthalpy method: benchmark solutions and magmatic focusing at mid-ocean ridges, *J. Petrol.*, 49(12), 2099–2121.
- Katz, R.F., 2010. Porosity-driven convection and asymmetry beneath mid-ocean ridges, Geochem. Geophys. Geosyst., 11(11), Q0AC07, doi:10.1029/2010GC003282.
- Katz, R.F. & Takei, Y., 2013. Consequences of viscous anisotropy in a deforming, two-phase aggregate. part 2. numerical solutions of the full equations, J. Fluid Mech., 734, 456–485.
- Katz, R.F., Spiegelman, M. & Langmuir, C.H., 2003. A new parameterization of hydrous mantle melting, *Geochem. Geophys. Geosyst.*, 4(9), 1073, doi:10.1029/2002GC000433.
- Katz, R.F., May, D., Rees Jones, D. & Tian, M., 2017. The subduction framework utilising scientific computing (subfusc)-an open-source simulation tool for two-phase dynamics of subduction zones, in AGU Fall Meeting Abstracts, American Geophysical Union.
- Keller, T., May, D.A. & Kaus, B. J.P., 2013. Numerical modelling of magma dynamics coupled to tectonic deformation of lithosphere and crust, *Geophys. J. Int.*, 195(3), 1406–1442.

- Keller, T., Katz, R.F. & Hirschmann, M.M., 2017. Volatiles beneath midocean ridges: deep melting, channelised transport, focusing, and metasomatism. Earth planet. Sci. Lett., 464, 55-68.
- Kronbichler, M., Heister, T. & Bangerth, W., 2012. High accuracy mantle convection simulation through modern numerical methods, *Geophys. J. Int.*, 191, 12–29.
- McKenzie, D., 1984. The generation and compaction of partially molten rock, *J. Petrol.*, **25**(3), 713–765.
- Miller, K.J., Zhu, W.-l., Montési, L.G. & Gaetani, G.A., 2014. Experimental quantification of permeability of partially molten mantle rock, *Earth planet. Sci. Lett.*, **388**, 273–282.
- Rhebergen, S., Wells, G.N., Katz, R.F. & Wathen, A.J., 2014. Analysis of block preconditioners for models of coupled magma/mantle dynamics, SIAM J. Sci. Comput., 36(4), A1960–A1977.
- Rhebergen, S., Wells, G.N., Wathen, A.J. & Katz, R.F., 2015. Three-field block preconditioners for models of coupled magma/mantle dynamics, SIAM J. Sci. Comput., 37(5), A2270–A2294.
- Rudge, J.F., 2018a. Textural equilibrium melt geometries around tetrakaidecahedral grains, Proc. R. Soc. A, 474(2212), 20170639.
- Rudge, J.F., 2018b. The viscosities of partially molten materials undergoing diffusion creep, J. geophys. Res., 123(12), 10–534.
- Schmeling, H., Kruse, J.P. & Richard, G., 2012. Effective shear and bulk viscosity of partially molten rock based on elastic moduli theory of a fluid filled poroelastic medium, *Geophys. J. Int.*, **190**(3), 1571–1578.
- Simpson, G., Spiegelman, M. & Weinstein, M.I., 2010. A multiscale model of partial melts: 2. Numerical results, J. geophys. Res., 115(B4).
- Sparks, D.W. & Parmentier, E., 1991. Melt extraction from the mantle beneath spreading centers, Earth planet. Sci. Lett., 105(4), 368–377.
- Spiegelman, M., 1993. Flow in deformable porous media. part 1 simple analysis, *J. Fluid Mech.*, **247**, 17–38.
- Spiegelman, M., Katz, R. & Simpson, G., 2007. An introduction and tutorial to the "McKenzie Equations" for magma migration, *Preprint, Columbia University, Dept. of Applied Physics and Applied Mathematics*, https://wiki.geodynamics.org/\_media/wg:magma\_migration:benchmark:1\_katz\_2007.pdf.
- Takei, Y. & Holtzman, B.K., 2009. Viscous constitutive relations of solid-liquid composites in terms of grain boundary contiguity: 1. Grain boundary diffusion control model, J. geophys. Res., 114(B6).
- Turner, A.J., Katz, R.F., Behn, M.D. & Keller, T., 2017. Magmatic focusing to mid-ocean ridges: the role of grain-size variability and non-newtonian viscosity, *Geochem. Geophys. Geosyst.*, 18(12), 4342–4355.
- Weatherley, S.M. & Katz, R.F., 2010. Plate-driven mantle dynamics and global patterns of mid-ocean ridge bathymetry, *Geochem. Geophys. Geosyst.*, **11**(10).
- Weatherley, S.M. & Katz, R.F., 2012. Melting and channelized magmatic flow in chemically heterogeneous, upwelling mantle, *Geochem. Geophys. Geosyst.*, **13**(5), Q0AC18, doi:10.1029/2011GC003989.
- Wilson, C.R., Spiegelman, M., van Keken, P.E. & Hacker, B.R., 2014. Fluid flow in subduction zones: the role of solid rheology and compaction pressure, *Earth planet. Sci. Lett.*, **401**, 261–274.
- Zhu, W. & Hirth, G., 2003. A network model for permeability in partially molten rocks, Earth planet. Sci. Lett., 212(3-4), 407-416.